

Microbeam Hard X-ray Photoemission Study on Platinum-group Metal Pernitrides

Kazuo Soda^{1,2*}, Tatsuya Mizui¹, Mai Komabuchi¹, Masahiko Kato¹,
Toshiki Terabe³, Kentaro Suzuki³, Ken Niwa³, Yuichi Shirako³, Masashi Hasegawa³,
Masaki Akaogi⁴, Hiroshi Kojitani⁴, and Eiji Ikenaga⁵

¹*Department of Quantum Engineering, Graduate School of Engineering, Nagoya University,
Furo-cho, Chikusa-ku, Nagoya 464-8603 Japan*

²*Synchrotron Radiation Research Center, Nagoya University,
Furo-cho, Chikusa-ku, Nagoya 464-8603 Japan*

³*Department of Crystalline Materials Science, Graduate School of Engineering,
Nagoya University, Furo-cho, Chikusa-ku, Nagoya 464-8603 Japan*

⁴*Department of Chemistry, Faculty of Science, Gakushuin University,
1-5-1 Mejiro, Toshima-ku, Tokyo 171-8588 Japan*

⁵*Japan Synchrotron Radiation Research Institute,
1-1-1 Koto, Sayo-cho, Hyogo 679-5198 Japan*

(Received , 2016)

Using microbeam hard x-ray photoelectron spectroscopy, we clarified the valence-band electronic structures and chemical states of platinum-group metal (Ru, Ir, and Pt) pernitrides, which have been synthesized in supercritical nitrogen fluid under extremely high pressures and temperatures. Their nitrogen contents relative to the platinum-group metal are estimated to be 2 from the photoemission intensity, which is consistent with the studies reported to date. The observed valence-band structures agree quite well with theoretically predicted structures for the pyrite-type PtN₂, arsenopyrite-type IrN₂, and marcasite-type RuN₂. The origin of their extremely large bulk moduli is discussed based on the current results of the valence-band structures and core-level chemical shifts.

1. Introduction

Synthesis under extremely high pressures and temperatures provides new materials whose compositions and crystalline structures differ from those produced under normal conditions, which thus possess novel properties and functions. Recently, it has been found that platinum-group metals ($M = \text{Pt, Ir, Os, Pd, Rh, and Ru}$) form their pernitrides via direct reactions with supercritical nitrogen fluid under such extreme conditions,¹⁻⁸⁾ which is noteworthy because no nitrides were known for the platinum-group metals to date. According

to X-ray diffraction (XRD) studies and electronic band-structure calculations,^{3,5,8-11)} Pt, Ir, and Ru, which are the subject of this research, form their pernitrides MN_2 of the pyrite-, arsenopyrite-, and marcasite-type structures, respectively. These pernitrides have respective large bulk moduli of 370, 428, and 330 GPa that are comparable to those of diamond (440 GPa) and TiN (320 GPa), which is a well-known hard material.¹²⁾ On the other hand, platinum-group metal compounds have also attracted considerable attention as $4d$ and $5d$ transition metal compounds, showing new physical properties and phenomena. In addition to on-site coulomb and charge-transfer interactions, their large spin-orbit interaction accounts for the formation of Weyl semimetals and topological insulators and superconductors.¹³⁻¹⁶⁾ Therefore, it is interesting to investigate the electronic structure and physical properties of the platinum-group pernitrides and compare them with those of other transition metal compounds.

These pernitrides comprise MN_6 polyhedra with N–N single covalent bonds, which may explain their large bulk moduli. In contrast, marcasite-type RuN_2 shows a relatively low bulk modulus, suggesting a relatively weak bonding interaction between N and Ru.⁸⁾ Theoretical calculations predict that the marcasite-type pernitrides have a metallic band structure, whereas other types of pernitrides are semiconductors.^{9,10)} For IrN_2 , the metal–insulator and structural phase transitions are expected.^{9,10)} However, the characterization of these pernitrides is hindered by the very tiny sizes, typically of 0.05 - 0.1 mm in diameter, of the pernitride specimens synthesized in a laser-heated diamond anvil cell.^{7,8)}

This research reports the direct investigation of the valence-band electronic structure and chemical states of the Ru, Ir, and Pt pernitrides via microbeam hard X-ray photoelectron spectroscopy (HAXPES) and discusses their physical properties.

2. Experimental

HAXPES measurements were performed at the beamline BL47XU of an 8-GeV electron storage ring, SPring-8, in an angle-dependent mode with a 7940-eV X-ray microbeam focused by a Kirkpatrick–Baez mirrors (vertical and horizontal widths of 0.8 and 2.6 μm , respectively) and recently developed electron input lens having a wide angular acceptance ($\pm 32^\circ$).^{17,18)} The origin of the binding energy E_B , *i.e.* the Fermi energy E_F , was determined by measuring the Fermi edges of a reference Au film deposited onto the sample holder, and the energy resolution was estimated as 0.27 eV. Specimens of the pernitrides were prepared by fiber-laser heating of the starting metals in a diamond anvil cell filled with supercritical nitrogen fluid.⁸⁾ The formation of the pernitrides was confirmed by XRD patterns and Raman

spectra. The XRD measurements also showed the patterns of the starting metals, which were residuals in the opposite side of the specimens to the incident laser.⁸⁾ The ambient recovered specimens and their starting metals were attached onto sharpened Cu pins with conductive epoxy glue. Due to the tiny specimen size, typically of $0.1 \times 0.1 \times 0.02 \text{ mm}^3$, no cleaning procedures were performed for the photoelectron measurement. The other experimental details were described in a previous study.¹⁹⁾ High-pressure phase PdF₂-type (HP-PdF₂-type) dioxides MO₂ were also measured as reference; they comprise corner-shared MO₆ octahedra with a nominal metal valence of +4.²⁰⁾

3. Results and Discussion

A typical HAXPES spectrum in a wide energy range of PtN₂ is compared with those of the starting Pt metal and HP-PdF₂-type PtO₂ in Fig. 1. Small C 1s lines and no O 1s signals are seen for the pernitride and metal specimens due to the surface contamination, while relatively large C 1s and small Cl 2s signals are found for the dioxide specimen. The Cl signal is observed probably due to accidental residual in the dioxide sample preparation procedures.²⁰⁾ Because of the insulating nature of reference PtO₂,²⁰⁾ the energy shift due to specimen charging is recognized and corrected by aligning the C 1s lines on the dioxide and metal, leading to the well alignment of the valence-band edge to E_F . This implied that HP-PdF₂-type PtO₂ may be a p-type semiconductor. Details of the experimental results of HP-PdF₂-type MO₂ will be reported elsewhere in the near future. With the theoretically calculated subshell photoionization cross sections,²¹⁾ the nitrogen contents relative to the platinum-group metal in the Ru, Ir, and Pt pernitrides are estimated with approximately 10% accuracy to be 2.1, 2.1, and 2.3 from the integrated intensity ratios of the N 1s core-level spectra relative to those of Ru 3d, Ir 4f, and Pt 4f spectra respectively. Here, the difference in the angular dependence of the differential photoionization cross sections of relevant core levels²²⁻²⁴⁾ is not considered. In fact, the angular dependences calculated using reported theoretical parameters²²⁻²⁴⁾ show that the nitrogen contents may be overestimated by approximately 10% without the angular dependences. Hence, we conclude that the nitrogen contents of the investigated pernitrides are 2 relative to the platinum-group metal. The estimated contents are consistent with those found in the literature.²⁻⁸⁾

Typical core-level spectra of the pernitrides together with those of the starting metals and reference dioxides are shown in Fig. 2. In this figure, the binding energy is relative to the lower binding-energy partner of the spin-orbit split pair of the metal, which is located at $E_B = 280.1, 60.8, \text{ and } 71.1 \text{ eV}$ for Ru 3d_{5/2}, Ir 4f_{7/2}, and Pt 4f_{7/2}, respectively. The Ir and Pt 4f_{7/2}

binding energies of their pernitrides are consistent with those previously reported.²⁾ Residual metal components of approximately 10% of the pernitrides are found for IrN₂ and PtN₂. Overlapping Ir 5*p*_{1/2} humps are also observed between Ir 4*f* lines, and partially overlapping Pt 5*p*_{1/2} features appear in the low binding-energy side of Pt 4*f* lines. A largely chemical-shifted pair observed for RuO₂ may be ascribed to the surface oxidation component RuO₃.^{25, 26)} Assuming a metal valence of +4 in the dioxides²⁰⁾ and the linear relation between valence and chemical shift, the nominal metal valences are estimated as -0.8, +4.3, and +3.6 from the observed chemical shifts of -0.11, +0.89, and +2.79 eV for Ru, Ir, and Pt pernitrides, respectively, and of +0.54, +0.82 and +3.06 eV for the respective oxides. The values for the Ir and Pt pernitrides are consistent with the presence of a N-N single-bond²⁷⁾ (they should be slightly corrected, because the experimental origin of the binding energy is set to the Fermi energy of the metallic Au reference; the Ir and Pt pernitrides are semiconductors, as discussed later). However, while large chemical-shifts toward the high binding-energy side, as in the case of their dioxides, indicate that either charge transfer from Ir and Pt to N or the decrease in valence electrons around both metallic elements in IrN₂ and PtN₂ occurs, a small shift toward the low binding energy side suggests a weaker Ru-N interaction or a more metallic nature in RuN₂.

The metallic asymmetric spectral profiles due to the multiple electron-hole excitation in the conduction band²⁸⁾ are also clearly observed for RuN₂, which agrees well with the valence-band spectrum of RuN₂ shown in Fig. 3, as well as for the starting metals Ru, Ir, and Pt and the metallic dioxides RuO₂ and IrO₂.²⁰⁾ Although the Pt 4*f*_{5/2} component of metallic Pt overlaps with the Pt 4*f*_{7/2} component of PtN₂, symmetric spectral profiles are found for IrN₂ and PtN₂, suggesting the semiconductor nature of these pernitrides in accordance with observations of their semiconductor-like valence-band spectra that are shown below.

On the other hand, the peak positions of N 1*s* lines are $E_B = 397.9, 398.6,$ and 399.1 eV for Ru, Ir, and Pt pernitrides, respectively. These lines were found to have an asymmetric spectral shape for metallic RuN₂ and symmetric spectral shapes for the semiconducting Ir and Pt pernitrides. The positive chemical shifts relative to the metallic Ru pernitride imply that the valence electrons are decreased around N in the semiconducting Ir and Pt pernitrides as compared with RuN₂.

Figure 3 shows the angle-integrated valence-band spectra of IrN₂ and RuN₂ together with their total and partial densities of states (DOS), which were calculated using the WIEN2k code²⁹⁾ in a framework of the full-potential linearized augmented plane wave (FLAPW)

method with the generalized gradient approximation proposed by Perdew, Burke, and Ernzerhof (GGA-PBE)³⁰⁾ and structural parameters reported in the literature⁹⁾. We employed 1000 k points in the Brillouin zone for self-consistent field cycle with the charge and energy convergences of 0.0001 e and 0.0001 Ry, respectively, and with the parameters of $R_{\text{MT}}K_{\text{max}} = 7$, $l_{\text{max}} = 7$, and $G_{\text{max}} = 12$. In the figure, the valence-band spectra are presented after subtracting the background due to the secondary electrons by an iteration method.³¹⁾ Although small O and C 1s signals due to the surface contamination are recognized in their wide energy-ranged spectra and the core-level spectra indicate a small metallic Ir component, the observed spectra agree quite well with the calculated DOS. In particular, a clear Fermi edge is observed for RuN₂, while a band edge of a p-type semiconductor, *i.e.*, gradual decrease in the intensity toward E_{F} , is found for IrN₂. Energy shifts due to the recoil effects are estimated to be 0.28, 0.04, 0.02, and 0.02 eV at most for N, Ru, Ir, and Au, respectively.³²⁾ Furthermore, the starting metals show almost no shifts of their Fermi edges. Thus, we successfully clarified metallic and semiconducting band structures predicted for marcasite-type RuN₂ and arsenopyrite-type IrN₂, respectively. At this point, it is noteworthy that the calculated valence-band width and the binding energy of the N 2s antibonding levels are smaller than the observed values by a factor of 0.92 - 0.95.

The top panel in Fig. 4 shows the angle-dependent valence-band spectra of the PtN₂ specimen, whose surface normal was set at an angle of 55° from the input lens axis. Their relation is schematically described in the literature.¹⁹⁾ Here, the emission angle θ is measured from the surface normal and the angle-dependent spectrum is obtained by summing up the spectral intensity within $\theta \pm 7.7^\circ$. The background due to the secondary electrons is also subtracted. A Fermi edge is clearly observed in both the bulk- and surface-sensitive spectra I_{b} and I_{s} recorded at $\theta = 29^\circ$ and 81° , respectively, and becomes prominent in the bulk-sensitive spectrum. Thus, the feature at E_{F} is attributed to the residual starting metal, whose valence-band spectrum is indicated by a solid curve in the bottom panel.

We decomposed the surface-sensitive spectrum I_{s} into the pernitride and metal components, which are represented by dots (with smoothed curve for the pernitride component) in the middle and bottom panels of Fig. 4, respectively, using the following relation:

$$\begin{pmatrix} I_{\text{b}} \\ I_{\text{s}} \end{pmatrix} = \begin{pmatrix} 0.12 & 0.88 \\ 0.09 & 0.91 \end{pmatrix} \begin{pmatrix} I_{\text{m}} \\ I_{\text{n}} \end{pmatrix}. \quad (1)$$

Here, I_{n} and I_{m} are the spectra of the pernitride and metal, respectively. The pernitride and metal fractions for the bulk- and surface-sensitive spectra are estimated from the

angle-dependent Pt $4f$ spectra under the assumption of having the same θ -dependence of the valence-band spectra.^{19, 33)} The decomposed PtN₂ spectrum is in good agreement with the calculated DOS, whose valence-band top is aligned arbitrarily at $E_B = 1$ eV, whereas the decomposed Pt component agrees fairly well with the measured Pt spectrum (solid curve in the bottom panel of Fig. 4). Thus, we directly showed the insulating or semiconducting valence-band structure for PtN₂, although there is a small and negative dip around E_F in the decomposed PtN₂ spectrum and a decrease in the second band of the decomposed Pt spectrum. These features probably arise from the uncertainties in the background estimation and subtraction of both the core-level and valence-band spectra, the decomposition of the core-level spectra into two spin-orbit pairs with overlapping Pt $5p_{1/2}$ humps, and the difference in the θ -dependence between the core-level and valence-band photoemissions.³⁴⁾ It is worth mentioning that it would be possible to minimize the θ -dependence due to the polarization of the excitation X-rays in the current experimental configuration,²⁴⁾ which would lead to a small change in the metal and pernitride fractions that could result in the elimination of the negative dip.

The middle panel in Fig. 5 shows this result with a slightly corrected relation, $I_s = 0.135 I_m + 0.875 I_n$, and its comparison with density of states calculated with the spin-orbit interaction. As shown in Fig. 5, the bands below $E_B \sim 7$ eV, particularly the main 4-eV band, are attributed mainly to the Pt $5d$ states, which are hybridized with the N $2p$ states, while the band between $E_B = 7 \sim 11$ eV arises from the N $2p$ states hybridized with the Pt $5d$ ones. In addition, the 15-eV hump is observed due to the antibonding N $2s$ band. The inclusion of the spin-orbit interaction leads to a better agreement between the experimental and theoretical results as the prominent peaks around $E_B = 4$ eV disappear with the resolution of the degeneracy. Overall, photoelectron spectral features resemble the Pt ($5d$) partial density of states because of the predominance of its photoionization cross section²¹⁾ and the valence-band maximum is shifted by approximately 0.6 eV toward the high binding energy. This shift indicates the existence of midgap states that fix the Fermi energy of the pernitride at approximately 0.6 eV, which is relative to metallic residual Pt and reference Au. Such midgap states may be caused by either surface or interface defects or by the topological surface state. From these results, we experimentally found from the core-level and valence-band spectra that pyrite-type PtN₂ has a semiconductor-like electronic band structure.

In the top panel of Fig. 5, the density of states calculated with the spin-orbit interaction for IrN₂ is compared with its experimental valence-band spectrum. The calculation with the

spin-orbit interaction improves the agreement with the experimental results. The calculated valence bands, particularly the main d band around 2 eV, broadened by approximately 0.1 eV.

As mentioned earlier, the observed spectral profiles and chemical shifts of their relevant core-levels suggest the deficiency in the valence electron around both metal element and nitrogen and thus the formation of covalent bonding in the semiconducting Ir and Pt pernitrides, compared with metallic RuN₂. Thus, as predicted, the directional and saturated single bonds of N–N and M –N cause the large bulk moduli for IrN₂ and PtN₂, while the weak Ru–N interaction and the non-directional nature of metallic bonds lead to the relatively low bulk modulus of RuN₂. At this point, it is interesting to compare the calculated electron density plots of both semiconductor-like PtN₂ and metallic RuN₂. As drawn by a code VESTA³⁵⁾ in Fig. 6, the charge density around one N atom in pyrite-type PtN₂ shows an equal connection to three neighboring Pt atoms and a relatively large connection to one N atom. Similarly, a Pt atom is equally connected to six neighboring N atoms with a covalent-bonding-like electronic density distribution. As reported in previous studies,^{4, 9, 27)} the N–N distances in PtN₂ and IrN₂ are increased from 0.11 nm, the typical value for the triple bond of a neutral N₂ molecule, to 0.14 nm, indicative of a single N–N covalent bond and nominal metal valence of +4. In PtN₂, the bond angles around N of Pt–N–Pt and Pt–N–N are 109.8° and 109.1°, respectively, which nearly resemble those of the tetrahedral sp^3 bonds in diamond (109.5°). Arsenopyrite-type IrN₂, which has the largest bulk modulus among the investigated pernitrides, shows an electronic density distribution same as that of PtN₂, although it is structurally distorted probably due to the interaction between the transition metal d and nitrogen states, as discussed for the $3d$ transition metal dichalcogenides.³⁶⁾ In marcasite-type RuN₂, the charge density around N reveals a stronger linkage with one Ru and one N along the b -axis than that with other two Ru atoms in the a – c plane but a weak Ru–N connection compared with PtN₂ because the charge density appears to be largely confined around an Ru atom and an N₂ molecular unit with a shorter N–N distance of 0.13 nm.⁸⁾ Overall, these features suggest the existence of a rigid directional Pt–N chemical bond and a more metallic non-directional Ru–N bond, which will be confirmed via high-resolution XRD analysis.

4. Conclusions

We experimentally clarified the valence-band electronic structures and chemical states of Ru, Ir, and Pt pernitrides, which were newly synthesized in high-pressure and

high-temperature supercritical nitrogen fluid, via microbeam HAXPES. Therefore, this technique will most probably serve as a useful analytical tool for the planetary and materials sciences as well as for material physics. The valence-band electronic structures can be well explained by the first-principle prediction for pyrite-type PtN₂, arsenopyrite-type IrN₂, and marcasite-type RuN₂. The observed chemical shifts and valence-band electronic structures point toward the semiconductor-like directional single covalent N–N and N–M bonds as the reason for the extremely high bulk moduli of PtN₂ and IrN₂.

Acknowledgments

This research was supported by JSPS KAKENHI Grant Number 25289219. The HAXPES experiments were conducted at BL47XU of SPring-8 with the approval of the Japan Synchrotron Radiation Research Institute (Proposal No. 2014A1160 and 2014B1112).

*E-mail: j45880a@cc.nagoya-u.ac.jp

- 1) E. Gregoryanz, C. Sanloup, M. Somayazulu, J. Badro, G. Fiquet, H.-K. Mao, and R. J. Hemley, *Nat. Mater.* **3**, 294 (2004).
- 2) J. C. Krowhurst, A. F. Goncharov, B. Sadigh, C. L. Evans, P. G. Morrall, J. L. Ferreira, and A. J. Nelson, *Science* **311**, 1275 (2006).
- 3) A. F. Young, J. A. Montoya, C. Sanloup, M. Lazzeri, E. Gregoryanz, and S. Scandolo, *Phys. Rev. B* **73**, 153102 (2006).
- 4) A. F. Young, C. Sanloup, E. Gregoryanz, S. Scandolo, R. J. Hemley, and H.-K. Mao, *Phys. Rev. Lett.* **96**, 155501 (2006).
- 5) J. A. Montoya, A. D. Hernandez, C. Sanloup, E. Gregoryanz, and S. Scandolo, *Appl. Phys. Lett.* **90**, 011909 (2007).
- 6) J. C. Krowhurst, A. F. Goncharov, B. Sadigh, J. M. Zaug, D. Aberg, Y. Meng, and V. B. Praksaenka, *J. Mater. Res.* **23**, 1 (2008).
- 7) K. Niwa, D. Dzivenko, K. Suzuki, R. Riedel, I. Troyan, M. Eremets, and M. Hasegawa, *Inorg. Chem.* **53**, 697 (2014).
- 8) K. Niwa, K. Suzuki, S. Muto, K. Tatsumi, K. Soda, T. Kikegawa and M. Hasegawa, *Chem.-Eur. J.* **20**, 13885 (2014).
- 9) R. Yu, Q. Zhan, and L. C. De Jonghe, *Angew. Chem. Int. Ed.* **46**, 1136 (2007).
- 10) E. R. Hernandez and E. Canadell, *J. Phys. Mater.* **18**, 2090 (2008).
- 11) D. Aberg, B. Sadigh, J. Crowhurst, and A. F. Goncharov, *Phys. Rev. Lett.* **100**, 095501 (2008).
- 12) R. Ahuja, O. Eriksson, J. M. Wills, and B. Johansson, *Phys. Rev. B* **53**, 3072 (1996).
- 13) S. Souma, Z. Wang, H. Kotaka, T. Sato, K. Nakayama, Y. Tanaka, H. Kimizuka, T. Takahashi, K. Yamauchi, T. Oguchi, K. Segawa, and Y. Ando, *Phys. Rev. B* **93**, 161112(R) (2016).
- 14) H. Weng, C. Fang, Z. Fang, B. A. Bernevig, and X. Dai, *Phys. Rev. X* **5**, 011029 (2015).
- 15) X. Wang, A. M. Turner, A. Vishwanath, and S. Y. Savrasov, *Phys. Rev. B* **83**, 205101 (2011).
- 16) X. L. Qi and S. C. Zhang, *Rev. Mod. Phys.* **83**, 1057 (2011).
- 17) H. Matsuda, H. Daimon, M. Kato, and M. Kudo, *Phys. Rev. E* **71**, 066503 (2005).
- 18) E. Ikenaga, M. Kobata, H. Matsuda, T. Sugiyama, H. Daimon, and K. Kobayashi, *J. Electron Spectros. Relat. Phenomena* **190**, 180 (2013).
- 19) K. Soda, H. Kondo, K. Yamaguchi, M. Kato, T. Shiraki, K. Niwa, K. Kusaba, M.

- Hasegawa, K. Xeniya, and E. Ikenaga, *J. Alloys Comp.* **643**, 195 (2015).
- 20) Y. Shirako, X. Wang, Y. Tsujimoto, K. Tanaka, Y. Guo, Y. Matsushita, Y. Nemoto, Y. Katsuya, Y. Shi, D. Mori, H. Kojitani, K. Yamaura, Y. Inaguma, and M. Akaogi, *Inorg. Chem.* **53**, 11616 (2014).
 - 21) J. J. Yeh and I. Lindau, *At. Data Nucl. Data Tables* **32**, 1 (1985).
 - 22) M. B. Trzhaskovskaya, V. I. Nefedov, and V. G. Yarzhemsky, *At. Data. Nucl. Data Tables* **77**, 97 (2001).
 - 23) M. B. Trzhaskovskaya, V. I. Nefedov, and V. G. Yarzhemsky, *At. Data. Nucl. Data Tables* **82**, 257 (2002).
 - 24) M. B. Trzhaskovskaya, V. K. Nikulin, V. I. Nefedov, and V. G. Yarzhemsky, *At. Data. Nucl. Data Tables* **92**, 245 (2006).
 - 25) K. S. Kim and N. Winograd, *J. Catal.* **35**, 66 (1974).
 - 26) Chemical shift database is found at <https://srdata.nist.gov/xps/Default.aspx>
 - 27) M. Wessel and R. Dronskowski, *J. Am. Chem. Soc.* **132**, 2121 (2010).
 - 28) S. Doniach and M. Sunjic, *J. Phys. C* **3**, 285 (1970).
 - 29) P. Blaha, K. Schwarz, P. Sorantin, and S. B. Trickey, *Comput. Phys. Commun.* **59**, 399 (1990).
 - 30) J. P. Perdew, K. Burke, and M. Ernzerhof, *Phys. Rev. Lett.* **77**, 3865 (1996).
 - 31) K. Soda, T. Mori, Y. Ōnuki, T. Komatsubara, S. Suga, A. Kakizaki, and T. Ishii, *J. Phys. Soc. Jpn.* **60**, 3059 (1991).
 - 32) C.S. Fadley, *J. Electron Spectros. Relat. Phenomena* **178-179**, 2 (2010).
 - 33) K. Soda, S. Ota, T. Suzuki, H. Miyazaki, M. Inukai, M. Kato, S. Yagi, T. Takeuchi, M. Hasegawa, H. Sato, and U. Mizutani, *AIP Conf. Proc.* **879**, 1821 (2007).
 - 34) A. Sekiyama, A. Higashiya, and S. Imada, *J. Electron Spectros. Relat. Phenomena* **190**, 201 (2013).
 - 35) K. Momma and F. Izumi, *J. Appl. Cryst.* **44**, 1272 (2011).
 - 36) J. B. Goodenough, *J. Solid State Chem.* **5**, 144 (1972).

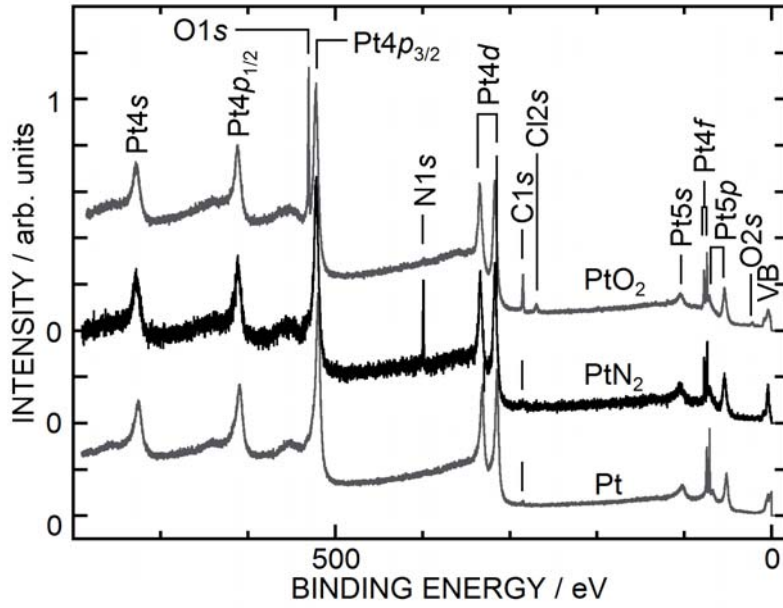


Fig. 1. Hard X-ray photoelectron spectra of Pt pernitride, starting Pt metal, and high-pressure phase PdF₂-type Pt dioxide.

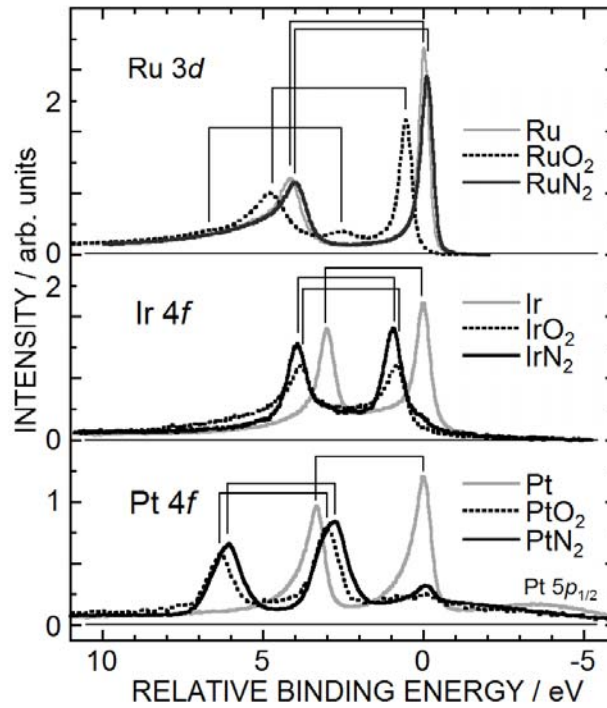


Fig. 2. Core-level spectra of Ru 3*d*, Ir 4*f*, and Pt 4*f* in their pernitrides (black curves), high-pressure phase PdF₂-type dioxides (dotted curves), and metals (gray curves). Spin-orbit pairs are indicated by linked bars.

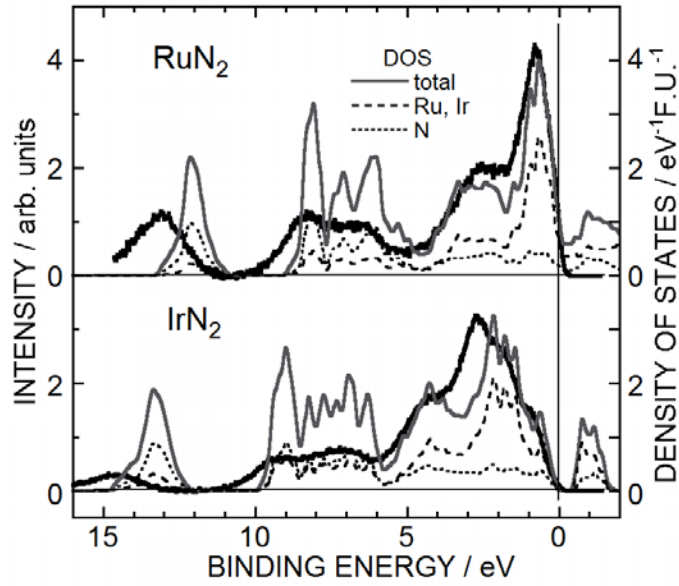


Fig. 3. Valence-band photoelectron spectra of Ru and Ir pernitrides. The background due to the secondary electrons was subtracted from the experimental photoelectron spectra. The theoretically calculated total (gray solid curve) and partial (broken and dotted curves) densities of states (DOS) are also shown for comparison.

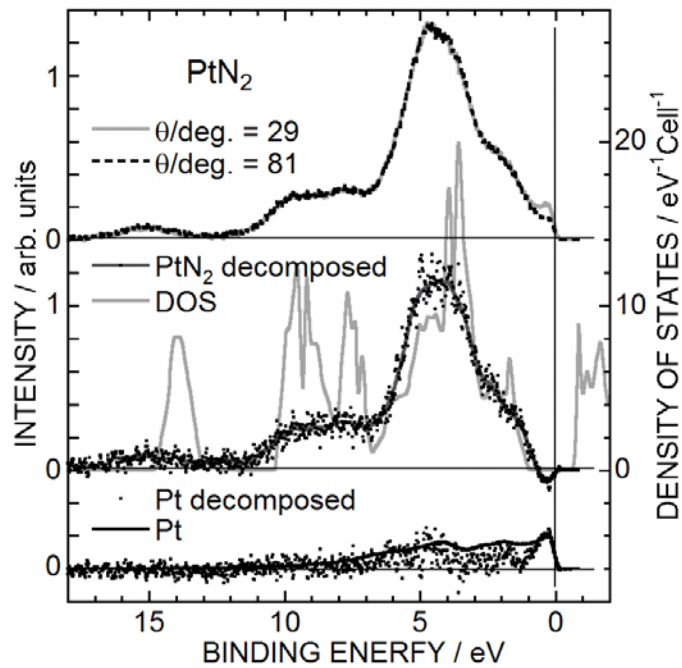


Fig. 4. The angle-dependent and decomposed valence-band spectra of PtN₂. The measured and decomposed valence-band spectra of Pt are also indicated by a solid curve and dots, respectively. The theoretically calculated density of states (DOS) is indicated by a gray curve for comparison.

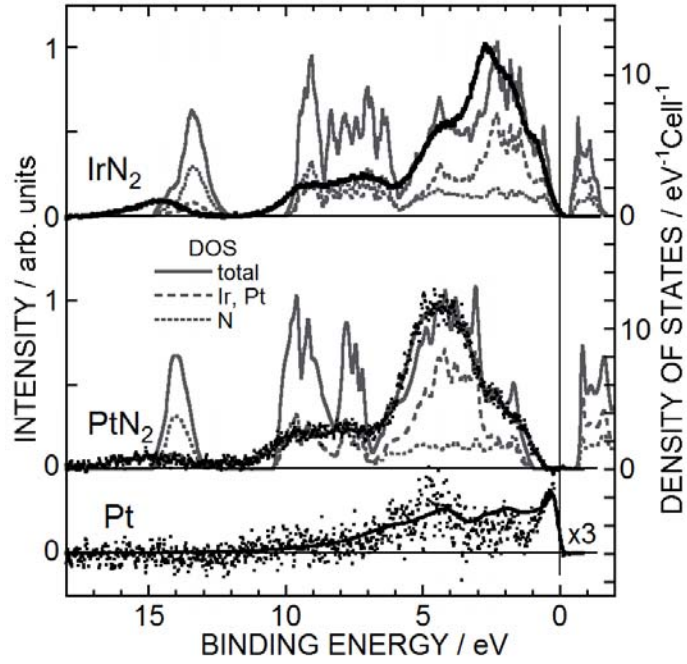


Fig. 5. Comparison between experimentally obtained valence-band spectra of IrN₂ (top panel) and PtN₂ (middle panel) and their densities of states (DOS) calculated with the spin-orbit interaction. For PtN₂, a decomposed valence-band spectrum and a Pt spectrum with an experimental Pt valence-band spectrum (bottom panel) are shown.

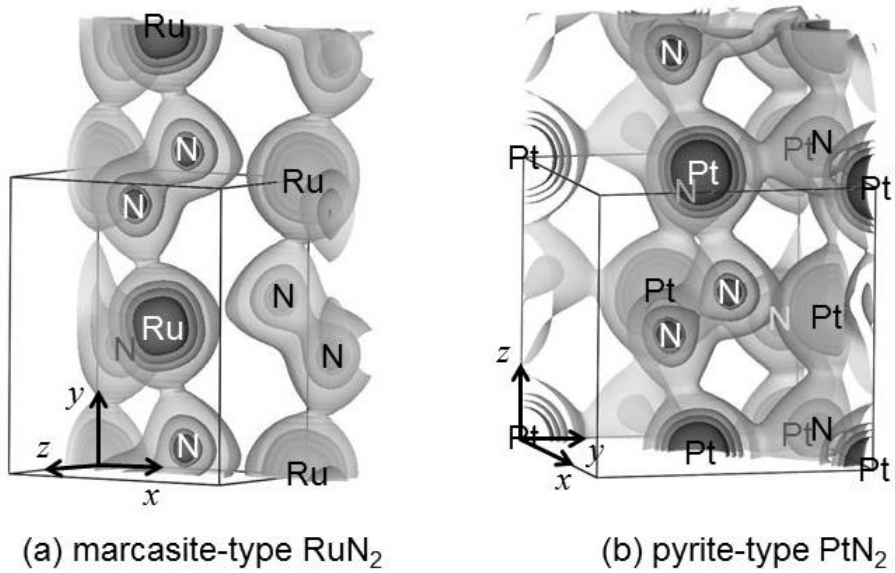


Fig. 6. Calculated electron density plots of (a) marcasite-type RuN₂ and (b) pyrite-type PtN₂. The electron density isosurfaces of 0.7, 2.1, 4.2, and 8.4 Å⁻³ with increasing darkness are drawn by a code VESTA³⁵. Cross sections cut in the (002) and (1-10) surfaces are shown for RuN₂ and PtN₂, respectively.